Probing Intracluster Magnetic Fields with Cosmic Microwave Background Polarization

Hiroshi Ohno[1,2], Masahiro Takada[3], Klaus Dolag[4], Matthias Bartelmann[4], and Naoshi Sugiyama[1]

ABSTRACT

Intracluster magnetic fields with $\sim \mu$G strength induce Faraday rotation on the cosmic microwave background (CMB) polarization. Measurements of this effect can potentially probe the detailed structure of intracluster magnetic fields across clusters, since the CMB polarization is a continuously varying field on the sky, in contrast to the conventional method restricted by the limited number of radio sources behind or inside a cluster. We here construct a method for extracting information on magnetic fields from measurements of the effect, combined with possible observations of the Sunyaev-Zel'dovich effect and X-ray emission for the same cluster which are needed to reconstruct the electron density fields. Employing the high-resolution magneto-hydrodynamic simulations performed by Dolag, Bartelmann & Lesch (1999) as a realistic model of magnetized intracluster gas distribution, we demonstrate how our reconstruction technique can well reproduce the magnetic fields, i.e., the spherically average radial profiles of the field strength and the coherence length.

1. Introduction

The origin and evolution of cosmic magnetic fields are still unclear and outstanding problems. Various observational techniques have consistently revealed that most clusters of galaxies are pervaded by magnetic fields of $B \sim$ O(1)μG strength (see e.g., Carilli &

[1]Division of Theoretical Astrophysics, National Astronomical Observatory, 2-21-1 Osawa, Mitaka, Tokyo 181-8588, Japan ; ohno@th.nao.ac.jp, naoshi@th.nao.ac.jp

[2]Research Center for the Early Universe, School of Science, University of Tokyo, Tokyo 113-0033, Japan ; ono@resceu.s.u-tokyo.ac.jp

[3]Department of Physics and Astronomy, University of Pennsylvania, 209 S. 33rd Street, Philadelphia, PA 19104, USA ; mtakada@hep.upenn.edu

[4]Max-Planck-Institut für Astrophysik, P.O. Box 1317, D-85741, Garching, Germany

Taylor 2002 for a review). Recently, Clarke, Kronberg & Böhringer (2001) have again drawn a robust conclusion that the intracluster hot plasma typically has a $B \sim 5 - 10$ μG field assuming a coherence length of 10kpc from the Faraday rotation measurements of 16 low-z ($z \leq 0.1$) clusters selected to be free of unusual radio halos. Since the rotation measure arises from the integration of the product of the electron density and the line-of-sight component of magnetic fields, it is generally difficult to extract information on the magnetic fields only from the rotation measure without introducing any assumptions on the gas distribution and the field configuration.

The first systematic study of the structure of magnetic fields over a single cluster was performed by Kim et al. (1991) based on the rotation measures of 18 sources close in angular position to the Coma cluster, giving the estimation of $B \sim 1\mu$G with the coherence length of 10kpc which is indicated from the magnetic field reversal scale. In a subsequent study, Feretti et al. (1995) discovered smaller coherence lengths down to 1 kpc from the rotation measures of the extended radio galaxy near the Coma cluster center, whereby the field strength estimation was modified to $B \sim 10\mu$G to explain the measured rotation angle. Thus, it is crucial for estimating the magnetic field strength robustly to determine the magnetic field coherence length which does not necessarily match the coherence length of the rotation measures. To study the detailed structure of the intracluster magnetic fields for any clusters, the high-resolution measurements of the Faraday rotation should at least be performed. However, there are some limitations for the conventional methods because of the lack of the number of radio sources behind or inside a cluster and possible contributions of the intrinsic Faraday rotation. Moreover, we should break the degeneracy of the rotation measure between the electron density and the magnetic field strength using some additional information for estimating the magnetic field strength.

Recently, Takada, Ohno & Sugiyama (2001) proposed that the magnetized intracluster gas similarly induces a Faraday rotation effect on the linearly polarized radiation of the cosmic microwave background (CMB) generated at the decoupling epoch of $z \approx 1000$ (see e.g., Hu & White 1997 for a study of the primary CMB polarization). They calculated the angular power spectra of this secondarily induced polarization under the simple assumption of a uniform field strength with $\sim 0.1\mu$ G across a cluster and suggested that the measurements could be used to set constraints on the average properties of the intracluster magnetic fields. Cooray, Melchiorri & Silk (2002) computed the secondary power spectrum including a circularly polarized contribution characterized by the Stokes-V parameter that is induced by possible relativistic plasma in clusters via the Faraday rotation. However, as a more interesting and realistic possibility, one may imagine that the secondary effect can be in principle used to map the detailed structure of the magnetic fields in an individual cluster, since the CMB polarization is a continuously varying field on the sky. In this paper, therefore, we study a method for reconstructing the magnetic fields from measurements of the Faraday rotation effect on the CMB polarization, combined with accessible observations of the Sunyaev-Zel'dovich (SZ) effect and X-ray emission for the same cluster to reconstruct the electron density distribution. For this purpose, it is crucial to consider a realistic magnetic field configuration as well as a plausible gas distribution as suggested by the currently favored formation scenario of galaxy clusters. Hence, as for a model of the magnetized cluster, we here employ high-resolution magneto-hydrodynamic simulation results performed by Dolag, Bartelmann & Lesch (1999), whereby we can simulate maps of the CMB polarization including the Faraday rotation effect as well as maps of the SZ effect and the thermal X-ray emission. Using those simulated maps, we demonstrate how well our method can reconstruct the magnetic fields. In particular, we try to clarify the relationship between the coherence lengths of the magnetic fields and the rotation measure. The coherence length should give a new insight into the nature and evolutionary history of magnetic fields. For example, if the magnetic fields have the coherence scale as large as or larger than the cluster size, the seed fields should be generated at the early stage of the universe (see e.g., Grasso and Rubinstein 2001 for a review), while smaller coherence lengths may imply the seed fields originated from galaxies within the cluster (e.g., Kronberg 1999).

This paper is organized as follows. In §2, we refer to the cluster models which are used to demonstrate the magnetic field reconstruction. In §3, we briefly review the primary CMB polarization map generated at the decoupling epoch and the Faraday rotation effect. In §4, assuming spherical symmetry of clusters, we show a method for reconstructing the density fields of the clusters from SZ effect and thermal X-ray emission which are directly calculated from simulated clusters. In §5, we develop a way to reconstruct the coherence length and strength of the magnetic fields combined with the previously reconstructed electron density fields. Finally, §6 is devoted to a summary and discussion.

2. Cluster models

We employ high-resolution magneto-hydrodynamic simulations performed by Dolag et al. (1999) as a realistic model of magnetized clusters. The simulations start from the seed magnetic field with 10^{-9}G strength, which is an upper limit to IGM fields set by Faraday rotation measurements of high-z radio loud QSOs (Kronberg 1996; Blasi, Burles, & Olinto 1999). They considered the homogeneous or chaotic field configurations for the initial seed fields, which are motivated by expectations of the primordial or galactic-wind induced initial seed fields, respectively. Then, the evolutionary history of the magnetic field was followed under the ideal magneto-hydrodynamic approximation. Several interesting results

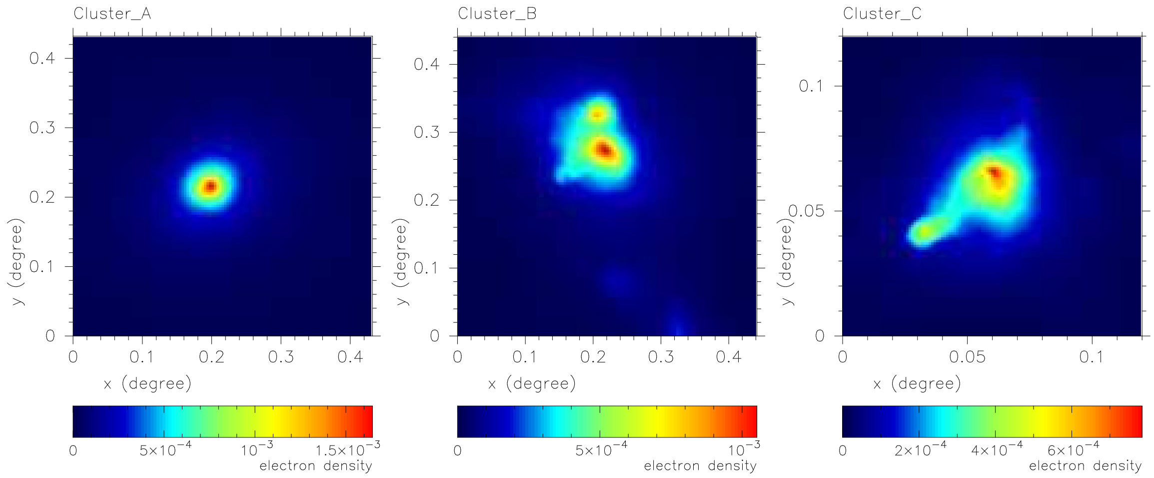

Fig. 1.— Average electron density along the line of sight, $\langle n_e(1/cm^3)\rangle \equiv 1/(2L)\int_{-L}^{L} ds n_e$ for each cluster (A, B, and C). The axes x and y show the angular scale in degrees.

Table 1. Cluster Models

	$ClusterA$	$ClusterB$	$ClusterC$
z	0.125	0.125	0.452
$r_{\rm vir}$ [kpc] [a]	666	700	500
$M_{\rm vir}$ [$M_\odot$]	3.5×10^{14}	2.5×10^{14}	2.4×10^{14}

[a] The centers of the clusters are taken at the electron density peaks.

were revealed in their paper. First, the initial field configurations are not important for field configurations in the final stage of cluster evolution. Secondly, the final field strength is amplified to reach 1μG by gravitational collapse and shear flows which induce Kelvin-Helmholtz instabilities. Although the simulation ignored effects associated with individual galaxies in the cluster on the evolution of the magnetic field, it is worth mentioning that the simulation results can explain some observational implications of the rotation measure (also see Dolag et al. 2001).

In the following, we consider the three typical simulated clusters (hereafter we refer to them as model A, B and C) for demonstrating the magnetic field reconstruction. Fig. 1 shows the average electron density $\langle n_e \rangle$ along the line of sight s, $\langle n_e \rangle \equiv 1/(2L) \int_{-L}^{L} ds n_e$, where $2L$ (= 4 Mpc) denotes the size of the simulation volume. The redshifts z, virial radii $r_{\rm vir}$, and virial Masses $M_{\rm vir}$ of the clusters are given in Table 2. The electron density distribution of model A looks spherically symmetric. Since the main amplification mechanism in the simulation is gravitational collapse, the magnetic field strength should be roughly in proportion to the electron density. Thus, we expect that the distribution of magnetic field strength can be also roughly considered as spherically symmetric. For this cluster model, therefore, the spherical symmetry approximation, which is a basic assumption for the following reconstructions, would be appropriate for both the magnetic field strength and the electron density. Model B has two density peaks in the cluster inner region, and the ratio of these peaks is ~ 1 . Hence, as a result of our analysis which takes the electron density peak as the cluster center, the reconstructed quantities may deviate from the spherically averaged true values around the second peak. Model C has a subcluster in the outskirts region, and the spherical symmetry assumption may not be appropriate for this cluster around the subcluster. Thus, the B and C clusters are considered to demonstrate how our method can work well for clusters with substructures. Note that the redshift of C cluster is higher than those of the other two clusters, which is the one reason of the elongated structure, and the simulation sequence indeed shows that the subcluster is merged with the main cluster component at the lower redshift. It should be again stressed that we will take the cluster centers as the electron density peaks in the following analysis.

3. Rotation measure and primary polarization

3.1. Small scale limit approximation of the Stokes parameters

Since the Faraday rotation effect due to the magnetized clusters on the CMB polarization is important only on the small angular scales, we can safely employ the small angle approximation (Zaldarriaga & Seljak 1998; Takada et al. 2001). In this limit, the Q and U

fields of the Stokes parameters can be expressed using the two-dimensional Fourier transformation in terms of the electric (E) and magnetic (B) modes (Kosowsky 1996; Zaldarriaga, & Seljak 1997;Kamionkowski, Kosowsky, & Stebbins 1997 a,b; Hu, & White 1997 a,b) as

$$\begin{aligned} Q(\boldsymbol{\theta}) &= \int \frac{d^2\boldsymbol{l}}{(2\pi)^2} \left[E_{\boldsymbol{l}} \cos 2\phi_{\boldsymbol{l}} - B_{\boldsymbol{l}} \sin 2\phi_{\boldsymbol{l}}\right] e^{i\boldsymbol{l}\cdot\boldsymbol{\theta}}, \\ U(\boldsymbol{\theta}) &= \int \frac{d^2\boldsymbol{l}}{(2\pi)^2} \left[E_{\boldsymbol{l}} \sin 2\phi_{\boldsymbol{l}} + B_{\boldsymbol{l}} \cos 2\phi_{\boldsymbol{l}}\right] e^{i\boldsymbol{l}\cdot\boldsymbol{\theta}}, \end{aligned} \tag{1}$$

where $\boldsymbol{l}$ and ϕ_l are defined as $\boldsymbol{l} \equiv l(\cos\phi_{\boldsymbol{l}}, \sin\phi_{\boldsymbol{l}})$ in the fixed (x,y)-orthogonal coordinates. Here, $E_{\boldsymbol{l}}$ and $B_{\boldsymbol{l}}$ are the Fourier coefficients for the primary E- and B-modes, respectively. We use the CMBFAST code (Seljak & Zaldarriaga 1996) to generate $E_{\boldsymbol{l}}$, and ignore the B-mode for simplicity, since the vector- and tensor-mode primordial fluctuations that induce the B-mode have not so far been detected. Thus, under the assumption of Gaussian random fields, we can easily make a primary polarization map (e.g., see a method of making the primary CMB temperature map in Takada & Futamase 2001 in more detail).

3.2. Faraday rotation

If a linearly polarized monochromatic radiation of frequency ν is passing through a hot plasma in the presence of magnetic fields along the propagation direction $\boldsymbol{s}$, the polarization vector will be rotated by the angle (the rotation measure), Δ_{RM} (see e.g., Rybicki & Lightman 1979);

$$\begin{aligned} \Delta_{RM} &= \frac{e^3}{2\pi m_e^2 c^2 \nu^2} \int ds n_e (\boldsymbol{B}\cdot\hat{\boldsymbol{s}}) \\ &\approx 8.12 \times 10^{-2} (1+z)^{-2} \left(\frac{\lambda_0}{1\ \mathrm{cm}}\right)^2 \int \frac{ds}{\mathrm{kpc}} \left(\frac{n_e}{1\ \mathrm{cm}^{-3}}\right) \left(\frac{\boldsymbol{B}\cdot\hat{\boldsymbol{s}}}{1\ \mu\mathrm{G}}\right), \end{aligned} \tag{2}$$

where λ_0 is the observed wavelength, and e and m_e denote the electron charge and mass, respectively. This Faraday rotation effect should rotate the primary CMB polarization vector as a secondary effect. From eq. (2), one can see that the rotation measure arises from the combined contributions of the electron density n_e and the line-of-sight component of the magnetic fields; $B_s \equiv \boldsymbol{B}\cdot\hat{\boldsymbol{s}}$. To break this degeneracy, we first consider a way to reconstruct the electron density fields in the next section. It is worth noting that the wavelength dependence could be used to separate the Faraday rotation effect from the primary CMB polarization and other secondary effects. Fig. 2 shows an example of the simulated CMB polarization maps with and without the secondary effect due to the Faraday rotation effect, where we have considered cluster A model.

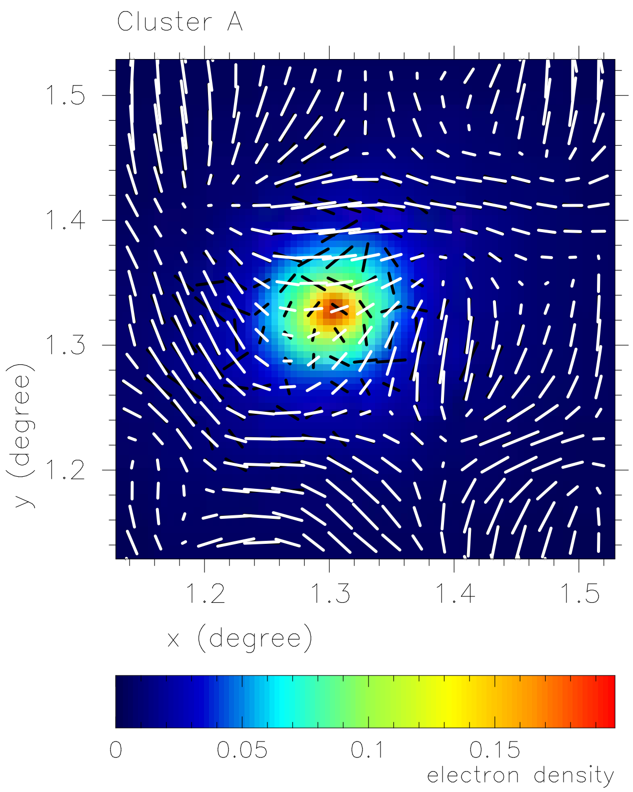

Fig. 2.— A example of the simulated map of the primary CMB polarization (white lines) and the map (black lines) including the Faraday rotation effect for cluster A model. The map is overlapped with the average density fields along the line of sight, $\langle n_e(\mathrm{cm}^{-3})\rangle \equiv 1/(2L)\int_{-L}^{L} ds n_e$ as in Fig. 1. The axes x and y show the angular scale in degrees.

4. Reconstruction of n_e

To break the degeneracy between $B_{||}$ and n_e in the rotation measure (2), we first consider a method for reconstructing electron density fields from possible observed maps of the X-ray surface brightness and SZ "flux", which can be produced directly from the simulation data of the clusters. We expect that typical clusters can be reasonably approximated as spherically symmetric bodies. Then, we can readily write down the X-ray surface brightness, S_X, and the Compton y parameter for the SZ effect, S_Y, at a given frequency band:

$$S_X(r') = A_X \int_{-\infty}^{\infty} n_e^2(r)\alpha(T_e)ds, \quad (3)$$

$$S_Y(r') = A_Y \int_{-\infty}^{\infty} n_e(r)T_e(r)ds, \quad (4)$$

where $s = \sqrt{r^2 - r'^2}$, r' and r denote the projected separation and spatial radius from the cluster center, respectively, and T_e is the electron temperature. Although we will use the physical scale r' throughout, S_X and S_Y can be also given by the angular separation θ from the center via the relation $r' = d_A\theta$, where d_A is the angular diameter distance to the cluster. Although A_X and A_Y can be computed once the observational frequency bands are specified, their explicit values and expressions are not relevant for the following analysis. Here, $\alpha(T_e)$ is the X-ray emissivity. We focus on the thermal bremsstrahlung only for simplicity and set $\alpha \propto \sqrt{T_e}$, although in reality one should take into account line emissions as well.

Under the spherical approximation, we can employ the Abel's integral to reconstruct electron density fields following the method developed by Yoshikawa & Suto (1999). Let us briefly summarize the concept. As in eq. (4), observable quantities $f(r')$ for clusters are often written as integrals of the corresponding three-dimensional quantities g along the line of sight as

$$f(r') = \int_{-\infty}^{\infty} g ds = 2\int_{r'}^{\infty} g \frac{rdr}{\sqrt{r^2 - r'^2}}. \tag{5}$$

If the quantity g depends on the radius r only (i.e. $g = g(r)$), we can use the Abel's integral to find

$$g(r) = \frac{1}{\pi}\int_{r}^{\infty} dr' \frac{df(r')}{dr'} \frac{r'}{\sqrt{r'^2 - r^2}}. \tag{6}$$

Thus, we can use this transformation formula to deproject the quantities in the clusters, assuming spherical symmetry. Applying the transformation above to $S_X(r')$ and $S_Y(r')$ given by eq. (4) yields

$$n_e^2(r)\sqrt{T_e} = \frac{1}{A_X\pi}\int_{r}^{\infty} dr' \frac{dS_X(r')}{dr'} \frac{r'}{\sqrt{r'^2 - r^2}}, \tag{7}$$

and

$$n_e(r)T_e(r) = \frac{1}{A_Y\pi}\int_{r}^{\infty} dr' \frac{dS_Y(r')}{dr'} \frac{r'}{\sqrt{r'^2 - r^2}}. \tag{8}$$

¿From the above two equations, the electron density can be reconstructed as

$$n_e(r) = \frac{\left(1/(A_X\pi)\int dS_X(r')r'/\sqrt{r'^2 - r^2}\right)^{2/3}}{\left(1/(A_Y\pi)\int dS_Y(r')r'/\sqrt{r'^2 - r^2}\right)^{1/3}}. \tag{9}$$

In the following, we demonstrate the performance of the above reconstruction technique. Since the simulated clusters are not spherically symmetric, we cannot directly apply eq. (9) to the simulation data and therefore performed the following procedure along the lines of the Abel's integral concept. We first computed the circularly averaged values of the simulated

$S_X(\boldsymbol{r}')$ and $S_Y(\boldsymbol{r}')$ in the annulus of a given projected radius r'. We then employed eq. (9) to the averaged S_X and S_Y, giving an estimation of the spherically averaged electron density profile. The left panel of Fig. 3 shows the averaged values of $S_X(r')$ and $S_Y(r')$ as a function of the projected radius r' calculated from the simulated maps of cluster model A, where the error denotes the 1 σ dispersion from the average value in each annulus (see also Yoshikawa & Suto 1999). Note that we do not attempt to include observational errors. The right panel of Fig. 3 plots the reconstructed electron density profile with 1σ error bars for cluster A. For the error assignment, we have constructed 200 realizations of the $S_X(r')$ and $S_Y(r')$ assuming Gaussian distributions of the errors at each bin, and then we calculated the average and 1σ dispersion from the reconstructed n_e in the realizations. It is apparent that the reconstructed density profile well matches the true spherically averaged profile of n_e directly computed from the simulation data. This is partly because cluster A model has no distinct substructure and the spherical approximation can be valid (see Fig. 1).

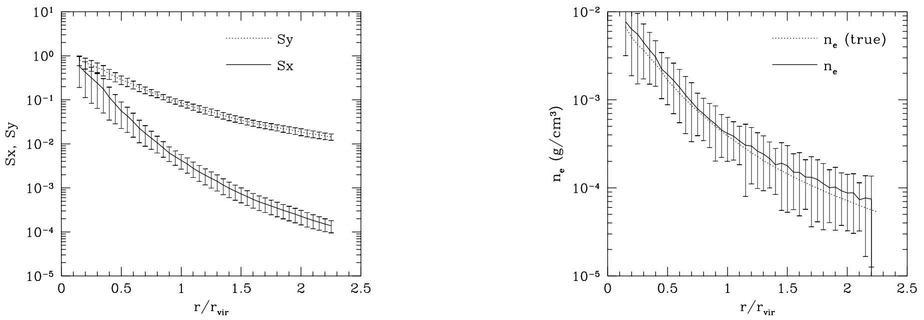

Fig. 3.— In the left panel, the upper line shows the normalized SZ y-parameter fields, S_Y, and the lower line denotes the normalized X-ray surface brightness, S_X, for cluster model A. The plotted values are the average values of those simulated quantities in the annulus of a given projected radius r', while the error bars show the 1σ deviation in the same annulus. The horizontal axis denotes the radius r normalized by the virial radius $r_{\rm vir}$. The right panel shows the reconstructed electron density n_e with $\pm 1\sigma$ errors (see text in more detail) and the true value of spherically averaged density profile directly obtained from the simulation.

5. Reconstruction of the Magnetic fields

Although one may imagine that the Abel's integral can be similarly applied to the reconstruction of the magnetic fields, it is not so easy as the reconstruction of the electron density fields, since the magnetic field is a vector quantity and various observations have implied the existence of reversal scale of the intracluster magnetic fields (e.g., Carilli & Taylor 2002). The magnetic fields will be treated like scalar quantities on scales below the coherence length where the directions of the magnetic fields are the same, and we therefore expect that the Abel's integral method can be effectively applied in order to estimate a typical field strength for the coherence scale. For this reason, we pay attention to developing a method for reconstructing the magnetic field strength as well as a way to estimate the coherence length from the observable quantity, i.e., the rotation measure. It should be again stressed that the magnetic field strength and the coherence length can be reconstructed as a function of the radius from the cluster center, which benefits from the fact that the CMB polarization field is a continuously varying field on the sky, if the secondary effect can be measured.

5.1. The dispersion of the rotation measure

To apply the Abel's integral to the observed rotation measure, we consider a simplest model of tangled magnetic fields; we assume that the magnetic field strength and the coherence length depend only on the radius from the cluster center. Even for this case, we should generally consider the random orientations of the magnetic fields for each cell with the coherence length, whereas the rotation measure along any line of sight can be regarded as the random walk process. Hence, the rotation measure in the direction of the projected radius r' can be expressed as a sum of the contributions from N cells along the line of sight;

$$\Delta_{RM}(\boldsymbol{r}') = \sum_{n}^{N} n_{e,n} l_n |B_n| \cos\chi_n. \tag{10}$$

where χ represents the angle between the magnetic field direction and the line of sight. Following the method developed by Lawler & Dennison (1982), the expectation value of the rotation measure in the annulus is zero and the 1 σ dispersion, $\sigma_{RM}(r')$, can be estimated as

$$\begin{aligned} \sigma_{RM}^2(r') &= \sum_{n}^{N}\sum_{m}^{M}\langle n_{e,n} l_n |B_n| \cos\chi_n \times n_{e,m} l_m |B_m| \cos\chi_m\rangle, \\ &= \frac{1}{3}\sum_{n}\left(l_n|B_n|n_{e,n}\right)^2, \\ &= \frac{2}{3}\int_{r'}^{\infty}\frac{rdr}{\sqrt{r^2-r'^2}} l(r) n_e^2(r) B^2(r), \end{aligned} \tag{11}$$

where in the second equation we have used $\langle\cos^2\chi_n\rangle = 1/3$ because of the random orientations of the magnetic fields for each cell. Since we can have a sufficient number of cells at a large separation r', eq. (11) is likely to give a good approximation because of the central limit theorem. Interestingly, eq. (11) allows us to use the Abel's integral (see eq. (6)) in order to obtain the field strength;

$$B^2(r) = \frac{3}{\pi} \frac{1}{l\,(r)\, n_e^2\,(r)} \int_r^\infty \frac{d\sigma_{RM}^2}{dr'} \frac{r' dr'}{\sqrt{r'^2 - r^2}}. \tag{12}$$

This equation means that the magnetic field strength can be estimated from the rotation measure once the coherence length and the electron density profile are given. Therefore, the next thing we should do is to consider a method for estimating the coherence length from the rotation measure fields.

5.2. Coherence length of magnetic fields

The two-point correlation function will be a useful and simplest quantity to estimate the coherence length of the magnetic fields. Let us first consider the two-point correlation function of the magnetic fields, which can be directly computed using the simulation data. From the meaning of the rotation measure, we here concentrate on the line-of-sight component of the magnetic fields, B_s. The the two-point correlation function of B_s, ξ_{B_s}, can be properly defined as

$$\xi_{B_s}(r'|r) \equiv \frac{\langle B_s(\boldsymbol{x}+\boldsymbol{y}) B_s(\boldsymbol{x}) \rangle_{|\boldsymbol{x}|=r, |\boldsymbol{y}|=r'}}{\langle B_s^2(\boldsymbol{x}) \rangle}, \tag{13}$$

where $\boldsymbol{x}$ and $\boldsymbol{x}+\boldsymbol{y}$ represent the three-dimensional position vectors from the cluster center and $\langle \ldots \rangle$ denotes the average among all possible pairs within the considered cluster subjected to the conditions of $|\boldsymbol{x}| = r$ and $|\boldsymbol{y}| = r'$. Note that, from our definition of ξ, we have $\xi_{B_s}(r' = 0|r) = 1$. Around a radius r from the cluster center, the two points, which are separated by more than the coherence length l, are considered to be uncorrelated because of the random field orientations, leading to $\xi_{B_s} \approx 0$ for $r' \gtrsim l$. Then, the coherence length at a given radius r will be roughly estimated from r' that satisfies the condition $\Delta\xi_{B_s}(r|r') = -1$. We can thus define the coherence length of magnetic fields as a form of the differentiation of the correlation function;

$$\frac{1}{l(r)} \equiv \left. \frac{-\Delta\xi(r'|r)}{\Delta r'} \right|_{r'=0}. \tag{14}$$

Here, to determine $l(r)$ from the simulated clusters, linear fitting is applied where $\frac{1}{2} \leq \xi \leq 1$ in practice.

Likewise, we can define the two-point correlation function of the rotation measure fields as

$$\xi_{RM}(r'|r) \equiv \frac{\langle \Delta_{RM}(\boldsymbol{x}+\boldsymbol{y})\Delta_{RM}(\boldsymbol{x})\rangle_{|\boldsymbol{x}|=r,|\boldsymbol{y}|=r'}}{\langle \Delta^2_{RM}(\boldsymbol{x})\rangle}, \tag{15}$$

where $\boldsymbol{x}$ represents the projection (2D) position vector in a circle of the radius r from the cluster center, and $\boldsymbol{y}$ represents a point in a circle of the radius r' from the vector $\boldsymbol{x}$. Although the correlation function of the rotation measures contains some information on the magnetic field coherence length, we should bear in mind that the magnetic field in the rotation measure is included not as a single field at a fixed point but as a summation of the fields weighted by the electron density along the line of sight. Thus, the two correlation functions of the magnetic fields and the rotation measures, ξ_{B_s} and ξ_{RM}, do not necessarily match each other.

Fig. 4 plots ξ_{B_s} and ξ_{RM} as a function of r' for cluster A model. We here show the results for $r/r_{\rm vir}$ = 0.015, 0.75, 1.25 and 2.15. Although it is not theoretically apparent whether these correlation functions match each other, these correlation functions seem to share the same properties. In fact, as shown in Fig. 5, the two coherence lengths that are estimated using eq. (14) from ξ_{B_s} and ξ_{RM} have almost the same features. This success can be explained as follows. The rotation measure arises mainly from the region near the cluster center because both the electron density and the magnetic field strength are relatively large there in the simulation data. Hence, the rotation measure is likely to reflect the property of the electron density fields and the magnetic fields on the plane which contains the cluster center. The magnetic fields determine the sign of the rotation measure because of the orientation dependence, and the electron density field is relatively a more smoothly varying function with respect to a radius than the magnetic fields. Thus, we could neglect the contribution of the density fields to the properties of the two-point correlation function of the rotation measure, and expect that the following relation roughly holds;

$$\xi_{B_s} \simeq \xi_{RM}. \tag{16}$$

In fact, we will see in §5.3 that this relation is also valid for B and C models of clusters. Then, without any additional observational quantities, we can reconstruct the magnetic field strength using the coherence length derived from the rotation measure, combined with the reconstructed electron density fields (see eq. (12)).

5.3. Results

We have presented a method for reconstructing the magnetic fields using the Abel integral (12) under the spherically symmetry assumption. In what follows, we demonstrate the performance of our method by comparing the reconstructed results with the true properties of the magnetic fields directly calculated from the simulation data. From eq. (12), we expect that our method gives the spherically averaged profile of $|B(\boldsymbol{r})|$ for a given radius, which is shown in the upper panel of Fig. 6 for cluster A model as in the left panel of Fig. 3. One can see that the averaged profile of $B(|\boldsymbol{r}|)$ is relatively noisy. This implies that the spherically symmetric assumption does not accurately hold for the simulated cluster. For this reason, we will also consider a following cumulative quantity as a radial profile;

$$I_B(r) \equiv \frac{\int d\Omega \int_0^r dr r^2 |\boldsymbol{B}(\boldsymbol{r})|}{\int_0^r dr 4\pi r^2}. \qquad (17)$$

Note that, to obtain the reconstructed profile of $I_B(r)$, we first reconstruct $B(r)$ using eq. (12) and then compute $I_B(r)$ using the equation above. The profile of $I_B(r)$ for cluster A model can be shown in the lower panel of Fig. 6, which implies that I_B is not so different from $B(r)$ because of its outer shell weighted form. The quantity $I_B(r)$ clarifies the tendency of the increasing or decreasing of the magnetic field strength due to its cumulative form.

Fig. 7 shows the reconstructed electron density fields, coherence lengths, magnetic field strengths and their cumulative quantities (I_B) for cluster models A, B and C.

Cluster A model is sufficiently virialized and we can consider spherical approximation as a reasonable assumption. As expected, all quantities of this cluster are well reconstructed. One can also see that the coherence length increases with radius r and the coherence length at the cluster center is small due to the large random motion of the fluid. The coherence length is an important property of the magnetic fields for reconstructing the magnetic field strength precisely from the rotation measure.

Cluster B model has two density peaks, and thus should be less virialized than the model A. Around the second peak ($r/r_{\rm vir} \sim 0.7$) of this cluster, the electron density is reconstructed larger than the true value directly calculated from the simulation data, because the circularly averaged X-ray and SZ fields in the annulus including the second density peak tend to give a reconstructed electron density larger than the spherically averaged density fields around the radius of the second peak (see eq. (9)). The coherence length of the rotation measure relatively matches the value of the magnetic field computed from the simulation data. Only around the second density peak where the random motion is large, however, the coherence length is reconstructed small relative to the true value. This may be because the random motion effect in the subcluster decreases the coherence length of the circularly averaged rotation measures more effectively than that of the spherically averaged magnetic fields. It should be noticed that the increase of the coherence length with radius is smaller than in cluster A. This may be due to the fact that in cluster B, which is less virialized than cluster A, the magnetic fields are not so efficiently tangled by the shear flow as in cluster A.

Although the magnetic fields are reconstructed with the density fields which deviate from the true value, the magnetic field strength seems to be well reconstructed. This is because the rotation measures which include the projected density fields show the same increase as the reconstructed density fields around the density peak, and the magnetic field strength is constructed from the ratio of these two values, which cancels out the increase of the density fields due to the second peak.

Besides having a subcluster, cluster C model is at the highest redshift among the three clusters. We therefore expect that the cluster is not as virialized as the other two clusters. In this cluster, the subcluster raises the reconstructed electron density near $r/r_{\rm vir} \sim 2.5$ as the result for cluster B around the second peak. The coherence length is reconstructed smaller than the true value around the subcluster, because the assumption of spherical symmetry is not appropriate as the result for cluster B model. We again stress that the relatively small slope of the coherence length with radius may be due to the insufficient virialization. In this case, the substructure in the outer region leads to the result that the magnetic field strength is reconstructed larger than the true value. This overestimation of the magnetic field strength is also caused by the deviation from the spherical symmetry due to the concentration of the magnetic field in the substructure. Nevertheless, it is interesting that the magnetic field strength is relatively well reconstructed at the inner range of a radius.

In total, the reconstructed profiles of the strength and coherence length of the magnetic fields agree with the true values for the three cluster models, in which the two clusters have the substructures in the inner and outer regions, respectively.

6. Conclusions

In this paper we have constructed a new method for reconstructing magnetic fields in galaxy clusters from the Faraday rotation effect on the CMB polarization, combined with possible observed maps of the X-ray emission and SZ effect on the CMB. Our results imply that the CMB polarization can be potentially used to reconstruct detailed radial profiles of the coherence length and strength of the magnetic fields. It was shown that the coherence length estimated from the rotation measure matches that of the magnetic fields. Therefore, we do not need any other information than the rotation measure for estimating the magnetic field coherence length. This coherence length is not only an important quantity for determining the magnetic field strength but also could reveal the origin of the initial seed fields.

To reconstruct the field strength, we consider the dispersion of the rotation measure fields in the annulus of a given projected radius, motivated by the random walk process caused by random orientations of the magnetic fields for a cell with the coherence length. However, the deviation of the field strength from the spherically averaged value may also increase the dispersion of the rotation measure, which we do not consider in this paper. This increase of the dispersion should lead to the increase of the reconstructed magnetic field strength. Nevertheless, the field strengths are well reconstructed in the three cluster models, and are reconstructed within a factor of a few even around the area where the dispersion of the field strength is large. Anyway, we expect that the method constructed in this paper will be a powerful tool for probing the intracluster magnetic fields.

Finally, we comment on the feasibility of this method. It is great challenging for current technology to detect the secondary effect of the intracluster magnetic fields on the CMB polarization. The rotation angle becomes about $1-10°$ at a frequency of 10GHz (e.g. $\Delta_{RM} \sim 1-10^{o}(10\mathrm{GHz}/\nu)^2$). The sensitivity of detector, which is needed to detect the Faraday rotation, is of order $1\,\mu K$. The angular resolution needed to reconstruct the structure of the magnetic fields is estimated from the minimum coherence length of the magnetic fields in the simulation cluster as $\sim$ 50kpc $\sim 20''$ (at z $\sim$ 0.1). The frequency dependence of the Faraday rotation can be also used to discriminate the effect from other secondary signals. Many observations are ongoing and planned for measuring the CMB polarization. We expect that future extensive observations of the CMB polarizations will allow reconstructions of intracluster magnetic fields with sufficient accuracy, which should give a crucial key to understanding the origin of intracluster magnetic fields.

We thank U.Seljak and M.Zaldarriaga for their available CMBFAST code. N.S. is supported by Japanese Grant-in-Aid for Science Research Fund of the Ministry of Education, No. 14540290. N.S. also acknowledges the people in Institut d'Astrophysique Spatiale, Universit'e Paris-Sud for their kind hospitality.

REFERENCES

Blasi, P., Burles, S., & Olinto, A.V. 1999, ApJ, 514, L79-82

Carilli, C.L., & Taylor, G. B. 2002, to appear in ARA&A, astro-ph/0110655

Clarke, T. E., Kronberg, P.P., & Böhringer, H. 2001, ApJ, 547, L111

Cooray, A., Melchiorri, A., & Silk, J. 2002, astro-ph/0205214

Dolag, K., Bartelmann, M., & Lesch, H. 1999, A&A, 348, 351

Dolag, K., Schindler, S., Govoni, F., & Feretti, L. 2001, A&A, 378, 777

Feretti, L., Dallacasa, D., Giovannini, G., & Tagliani, A. 1995, A&A, 302, 680

Grasso, D., & Rubinstein, H. 1995, Nuc.Phys.B, 43, 303-7

Hu, W.,& White, M. 1997, Phys. Rev. D, 56, 596

Hu, W.,& White, M. 1997, NewA, 2, 232

Kamionkowski, M., Kosowsky, A., & Stebbins, A. 1997, Phys. Rev. Lett., 78, 2058

Kamionkowski, M., Kosowsky, A., & Stebbins, A. 1997, Phys. Rev. D, 55, 7368

Kim, K.-T., Kronberg, P. P., Dewdney, P. E., Landecker, T. L. 1990, ApJ, 355, 29

Kim, K.-T., Tribble, P. C., & Kronberg, P. P. 1991, ApJ, 379, 80

Kosowsky, A. 1996, Ann.Phys.,246,49

Kronberg P.P. 1996, Space Science Reveiws, 75, 387-99

Lawler, J.M., & Dennison, B. 1982, ApJ, 252, 81

Rybicki, G.B., Lightman, A.P. 1979, Radiative Processes in Astrophysics (New York: John Wiley Sons)

Seljak, U., & Zaldarriaga, M. 1996, ApJ, 469, 437

Takada, M., & Futamase, T. 2001, ApJ, 546, 620

Takada, M., Ohno, H., & Sugiyama, N. 2001, astro-ph/0112412

Yoshikawa, K., & Suto, Y. 1999, ApJ,513,549

Zaldarriaga, M., Seljak, U. 1997, Phys. Rev. D, 55, 1830

Zaldarriaga, M., Seljak, U. 1998, Phys. Rev. D, 58, 023003

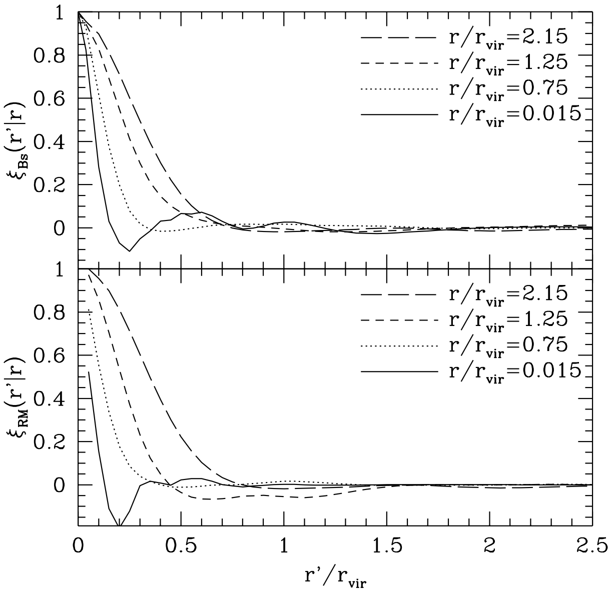

Fig. 4.— The upper panel shows $\xi_{B_s}(r'|r)$ for cluster A model, and the lower panel shows $\xi_{RM}(r'|r)$ for the same cluster. The correlation functions are plotted for each radius r which is the distance from the cluster center. The horizontal axis denotes the radius r' normalized by the virial radius $r_{\rm vir}$. Note that the radius parameters r' for ξ_{B_s} and ξ_{RM} are distances from a fixed point located in a sphere or circle of the radius r from the center of the cluster, respectively.

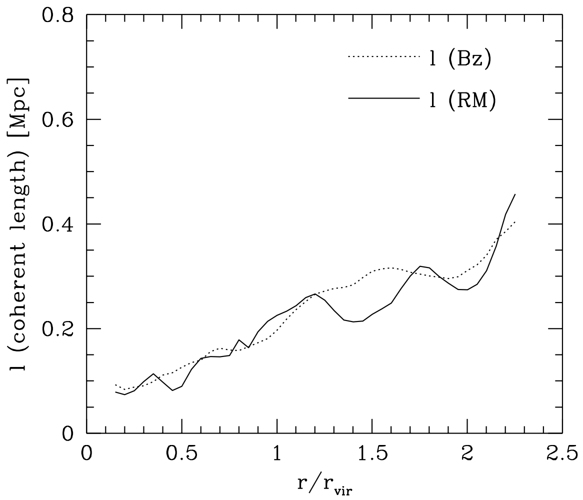

Fig. 5.— The coherence lengths of the magnetic fields in cluster A. The horizontal axis denotes the radius r normalized by the virial radius $r_{\rm vir}$. The dotted and solid curves show the results estimated from ξ_{B_s} and ξ_{RM} using eq. (14), respectively. Those coherence lengths well match each other at the considered range of a radius r.

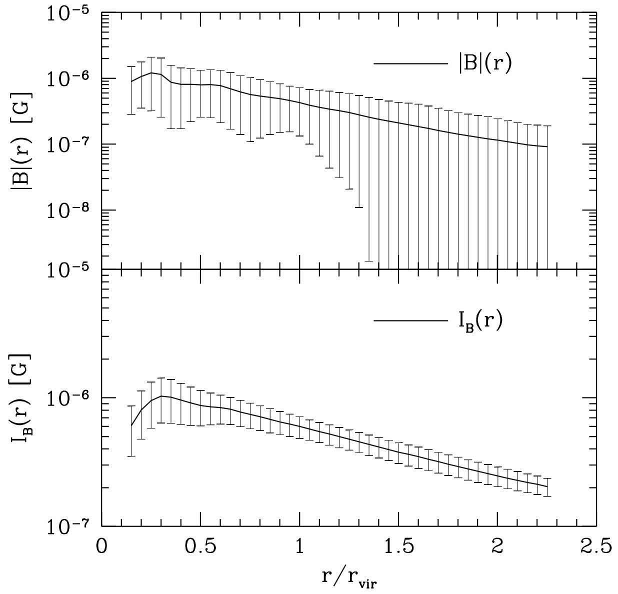

Fig. 6.— The upper panel shows the spherically averaged profile of $|B(\boldsymbol{r})|$ for cluster A model, where the error bars denote 1σ deviations from the average value for each bin of radius r as shown in Fig. 3. Similarly, the lower panel shows the cumulative field strength $I_B(r)[G]$, which is computed using eq. (17). The horizontal axes denote the radius r normalized by the virial radius $r_{\rm vir}$.

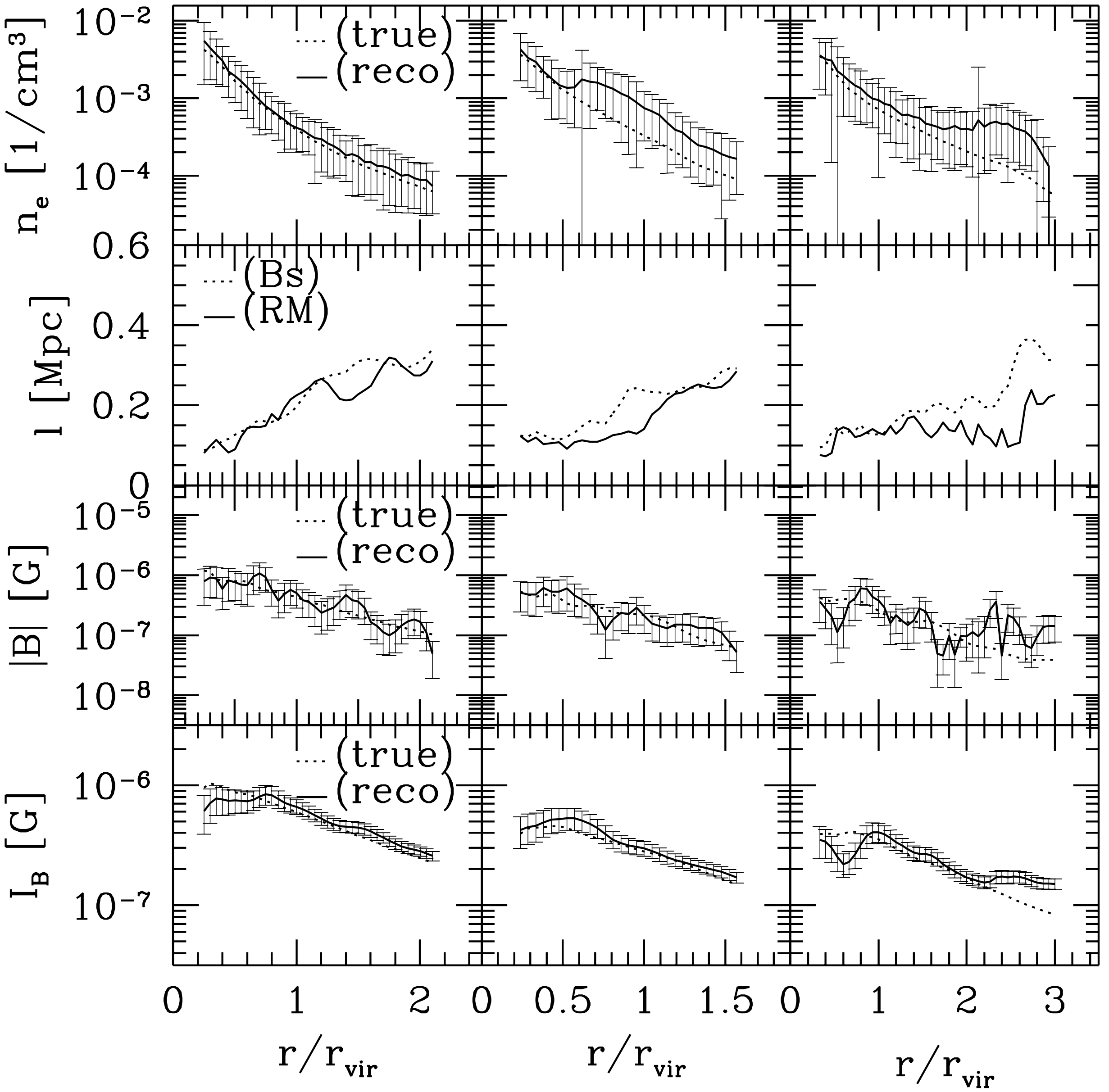

Fig. 7.— These panels show the comparisons of the reconstructed profiles of the electron densities, the coherence lengths, the magnetic field strengths and the cumulative field strengths with the true profiles computed from the simulation data. The left, middle and right panels are the results for clusters A, B, and C, respectively. The those quantities are reconstructed using equations (9), (14), (12) and (17), respectively.